



HAL
open science

Flow and Acoustic Fields of Rocket Jets Impinging on a Perforated Plate

Mathieu Varé, Christophe Bogey

► **To cite this version:**

Mathieu Varé, Christophe Bogey. Flow and Acoustic Fields of Rocket Jets Impinging on a Perforated Plate. *AIAA Journal*, 2022, 60 (8), pp.4614-4627. 10.2514/1.J061253 . hal-03636507

HAL Id: hal-03636507

<https://hal.science/hal-03636507>

Submitted on 10 Apr 2022

HAL is a multi-disciplinary open access archive for the deposit and dissemination of scientific research documents, whether they are published or not. The documents may come from teaching and research institutions in France or abroad, or from public or private research centers.

L'archive ouverte pluridisciplinaire **HAL**, est destinée au dépôt et à la diffusion de documents scientifiques de niveau recherche, publiés ou non, émanant des établissements d'enseignement et de recherche français ou étrangers, des laboratoires publics ou privés.



Flow and Acoustic Fields of Rocket Jets Impinging on a Perforated Plate

Mathieu Varé*^{ORCID} and Christophe Bogey†^{ORCID}

Laboratoire de Mécanique des Fluides et d'Acoustique, LMFA UMR 5509, 69130 Ecully, France

<https://doi.org/10.2514/1.J061253>

The flow and acoustic fields of jets at a Mach number of 3.1 impinging on a plate at $15D$ of the jet nozzle exit, where D is the nozzle diameter, have been investigated using highly resolved large-eddy simulations. The plate is perforated with a hole of diameter $h = 1.33D, 2D, 3D$, or $4D$. The full-plate and free-jet cases have also been considered. The pressure levels are highest for the non-perforated plate and decrease as the hole diameter increases. Compared with the free jet, they are higher by about 5 dB for the full plate, 4 dB for $h = 1.33D$ and $2D$, 3 dB for $h = 3D$, and 2 dB for $h = 4D$. In the upstream direction, the broadband shock-associated noise is prevailing for the free jet. For the impinging jets, the main noise component in that direction is produced by the impingement of the jet turbulent structures on the plate. In the downstream direction, for the free jet and down to the plate for the impinging jets, the sound field is dominated by Mach waves. Downstream of the perforated plates, waves are generated by interactions between the jet flow and the plate.

Nomenclature

c	=	speed of sound
D	=	nozzle diameter
f	=	frequency
h	=	hole diameter
k	=	wavenumber
L	=	nozzle-to-plate distance
L_s	=	shock cell length
M	=	Mach number, u/c
M_c	=	convection Mach number
N	=	number of grid points
n	=	mode number
p	=	pressure
\mathcal{R}	=	correlation coefficient
r_0	=	nozzle radius, $D/2$
(r, θ, z)	=	cylindrical coordinate system
St	=	diameter-based Strouhal number, fD/u_e
T	=	temperature
u	=	velocity
u_c	=	convection velocity
v_ϕ	=	wave phase velocity
W_d	=	sound power associated with the downstream-propagating waves
W_u	=	sound power associated with the upstream-propagating waves
z_c	=	potential core length
α	=	angle
Δr	=	radial mesh spacing
Δz	=	axial mesh spacing
δ	=	thickness of Blasius boundary-layer profile
δt	=	time delay
δ_θ	=	momentum thickness
λ	=	wavelength
ν	=	kinematic molecular viscosity
ρ	=	density

$\langle \rangle$	=	temporal averaging operator
$\tilde{}$	=	Fourier transform in directions r and z

Subscripts

e	=	nozzle-exit conditions
j	=	ideally expanded equivalent jet conditions
r	=	radial direction
z	=	axial direction
θ	=	azimuthal direction
0	=	ambient conditions

Superscript

$'$	=	fluctuation
-----	---	-------------

I. Introduction

DURING a rocket launch, the hot supersonic gases of the engines are canalized in a trench dug under the rocket. However, a part of the jets impinges on the ground, which generates intense acoustic waves. These waves propagate upstream to the fairing, where they might excite the rocket structure and damage the payload. Thus, the understanding of noise generation at the liftoff of a space launcher is a main concern for the aerospace industry.

To analyze noise generation during a rocket launch, a simplified geometry of a launch pad, namely, a jet impinging on a perforated plate, can be considered. Such a configuration has been investigated numerically by different researchers [1–3] for hot overexpanded supersonic jets, typical of rocket jets, for nozzle-to-plate distances L varying between $15D$ and $20D$, where $D = 2r_0$ is the nozzle diameter. In particular, Kawai et al. [1] studied the impingement of an overexpanded jet at an exit Mach number of 3.66 on a plate with a hole using an axisymmetric large-eddy simulation (LES). They observed a strong acoustic radiation in the upstream direction, which they identified as the reflections of the jet Mach waves on the plate. For a similar geometry, Tsutsumi et al. [2] simulated a jet at an exit Mach number of 3.7. They highlighted the presence of another significant upstream noise component, generated by the impingement of the jet turbulent structures on the hole edges. This component was also visualized in the acoustic far field of a jet at a Mach number of 3.1 impinging on a perforated plate in the simulations of Troyes et al. [3]. Nevertheless, it is still unclear which one of the two upstream components, the impingement noise or the reflected Mach waves, dominates. Moreover, the levels in the acoustic field mainly depend on two geometrical parameters, namely, the nozzle-to-plate distance L and the hole diameter h .

Presented as Paper 2021-2252 at the 27th AIAA/CEAS Aeroacoustics Conference, AIAA Aviation Forum, Virtual Event, August 2–6, 2021; received 3 September 2021; revision received 22 February 2022; accepted for publication 22 February 2022; published online 6 April 2022. Copyright © 2022 by the authors. Published by the American Institute of Aeronautics and Astronautics, Inc., with permission. All requests for copying and permission to reprint should be submitted to CCC at www.copyright.com; employ the eISSN 1533-385X to initiate your request. See also AIAA Rights and Permissions www.aiaa.org/randp.

*Postdoctoral Fellow; mathieu.vare@ec-lyon.fr.

†CNRS Research Scientist; christophe.bogey@ec-lyon.fr. Associate Fellow AIAA.

The effects of the nozzle-to-plate distance have been investigated in the simulations of a rocket launch by Tsutsumi et al. [4]. These authors considered a rocket with five jets impinging on a plate with five holes aligned with the jets for the four nozzle-to-plate distances of $6D$, $11D$, $16D$, and $21D$. The pressure levels near the jet nozzle were noted to be strongest for $L = 16D$. The influence of the hole has been examined by Tsutsumi et al. [2] for jets at a Mach number of 3.7. In their study, a free jet, a jet impinging on a flat plate, and three jets impinging on a plate with a hole of diameter $h = 2D$, $3D$, or $4D$ were computed. For all impinging jets, the nozzle-to-plate distance was equal to $20D$. The overall sound pressure levels were found to decrease as the hole diameter increases, with a reduction varying from 2 dB for $h = 2D$ up to 4 dB for $h = 4D$ compared with the flat-plate configuration. Despite the preceding works, several questions remain about the sound radiation of rocket jets impinging on a perforated plate. For instance, the existing studies mainly focus on the waves propagating in the upstream direction, but the radiation in the other directions has not been examined in depth. In the same way, the sound field downstream of the plate, the knowledge of which may be useful to understand the pressure field in the flame trench of a rocket launchpad, has not been detailed. In addition, the resolution of earlier numerical simulations is rather low, yielding a Strouhal cutoff number around 0.2 [2,3], which does not allow high-frequency noise components to be captured. Finally, in the studies on impinging jets at a Mach number lower than 2 [5–13], intense tones were also shown to be generated by feedback loops establishing between the nozzle exit and the plate. Such tones do not seem to emerge for Mach numbers around 3 [2,3], suggesting that there are no feedback loops or only weak ones in that case. However, the possibility of resonance phenomena has not been discussed thoroughly for impinging jets at these Mach numbers.

In the present work, the flow and acoustic fields of rocket jets impinging on a perforated plate are investigated. For that, six over-expanded supersonic jets at an exit Mach number M_e of 3.1 and a Reynolds number Re_D of 2×10^5 are simulated by LES. One jet is free, and the five other ones impinge on a plate located at a distance of $L = 15D$ from the nozzle exit. Four of the plates have a hole of diameter $h = 1.33D$, $2D$, $3D$, and $4D$, whereas the fifth one has no hole. The first objective in this study is to investigate the effects of the hole and its diameter on the sound radiated in the upstream direction. For that purpose, the jet flow and acoustic fields are described. In particular, the spectra of the pressure fluctuations in the vicinity of the nozzle are examined. The second objective is to identify the different components of the acoustic radiation. To this end, a two-dimensional spatial Fourier transform is applied to the acoustic pressure fields in order to highlight the main propagation directions of the sound

waves. Two-dimensional space–time correlations are also used to show the propagation of the acoustic waves upstream but also downstream of the plate. The last aim of this study is to discuss the establishment of possible feedback loops between the nozzle and the plate. To reveal such resonance phenomena, frequency–wave-number spectra of the pressure fluctuations are computed to identify the presence of upstream-propagating waves in the jet flow.

This paper is organized as follows. The jet parameters and numerical methods used in the LES are documented in Sec. II. The results of the simulations are presented in Sec. III. Finally, concluding remarks are given in Sec. IV.

II. Parameters

A. Jet Parameters

The parameters of the simulated jets are provided in Table 1. The jets have an exhaust Mach number $M_e = u_e/c_e$ of 3.1 and a Reynolds number $Re_D = u_e D/\nu_e$ of 2×10^5 , where u_e is the velocity, c_e is the sound speed, and ν_e is the kinematic viscosity at the jet nozzle exit. The exhaust temperature T_e is equal to 738 K and the exhaust pressure p_e is set to $0.63p_0$, where $p_0 = 10^5$ Pa is the ambient pressure. The parameters of the corresponding ideally expanded jet are also given in Table 1. In particular, the ideally expanded Mach number is equal to $M_j = 2.9$. The ejection parameters of the jets have been chosen to match those of a mixed hydrogen–air jet considered in experiments conducted at the MARTEL facility [14] and in the simulations of Troyes et al. [3]. The jet static temperature T_e is fixed so that the ratio c_e/c_0 between the local and the ambient sound speeds is identical to that in the hydrogen–air jet in the MARTEL experiments, following the approach of Doty and McLaughlin [15].

The first jet, labeled as jetfree, is free, whereas the second one, jeth0, impinges on a full plate. The four other ones, jeth1, jeth2, jeth3, and jeth4, impinge on a plate with a hole centered on the jet axis of diameter $h = 1.33D$, $2D$, $3D$, and $4D$, respectively. For the impinging jets, the nozzle-to-plate distance L is equal to $30r_0$. The nozzle-to-plate distance and the two hole diameters $h = 1.33D$ and $2D$ are the same as in the experiments [14]. Finally, the width e of the plates with a hole is arbitrarily chosen equal to r_0 .

The six jets exhaust from a cylindrical nozzle of length $2r_0$, at the inlet of which Blasius boundary-layer profiles with a thickness δ of $0.15r_0$ are imposed. Vortical disturbances non-correlated in the azimuthal direction are added in the pipe at $z = -r_0$ to trigger the boundary-layer transition from a fully laminar to a disturbed state [16]. The radial profiles of mean velocity and root-mean-square (rms) values of the axial velocity fluctuations thus obtained at the nozzle exit are plotted in Fig. 1. In Fig. 1a, the mean velocity profiles are very similar for the six jets. The mean velocity decreases slowly from u_e down to $\langle u_z \rangle = 0.93u_e$ at $r = 0.8r_0$, then is drastically reduced down to zero at $r = 0.9r_0$. The profiles appear to significantly differ from the boundary-layer profile imposed at the nozzle inlet, also represented. The discrepancies between the nozzle-exit and the nozzle-inlet profiles can be explained by the fact that near the nozzle exit, the boundary layer is slightly detached from the wall due to the over-expansion of the jets [17]. In Fig. 1b, for all jets, the radial profile of

Table 1 Jets parameters: exit Mach number M_e , pressure p_e , and temperature T_e and ideally expanded Mach number M_j , temperature T_j , and diameter D_j

M_e	p_e/p_0	T_e/T_0	M_j	T_j/T_0	D_j/D
3.1	0.63	2.5	2.9	2.2	0.9

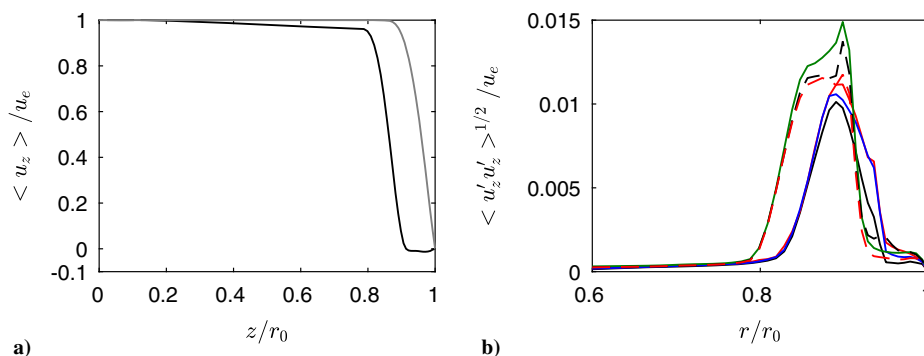


Fig. 1 Radial profiles of a) mean axial velocity $\langle u_z \rangle / u_e$ at — the nozzle exit and — at the nozzle inlet and b) axial turbulence intensity $\langle u'_z u'_z \rangle^{1/2} / u_e$ at the nozzle exit: — jeth0, — jeth1, — jeth2, - - - jeth3, - - - jeth4, and — jetfree.

rms velocity fluctuations reaches a peak value at $r \approx 0.9r_0$. The peak rms levels range between 1 and 1.5% of the exit velocity, indicating weakly disturbed nozzle-exit conditions.

B. Numerical Methods

The numerical setup is identical to that used in recent LES of subsonic and supersonic, free [18,19], and impinging [12,13] jets. In the simulations, the unsteady compressible Navier–Stokes equations are solved in cylindrical coordinates (r, θ, z) using an OpenMP-based in-house solver. The time integration is performed using a six-stage Runge–Kutta algorithm and the spatial derivatives are evaluated with eleven-point low-dispersion finite-difference schemes [20] ensuring high accuracy down to five points per wavelength. At the end of each time step, a selective filtering is applied to remove grid-to-grid oscillations [21]. This filter dissipates kinetic turbulent energy near the grid cutoff frequency, thus acting as a subgrid-scale model [22]. Solid and adiabatic wall conditions are implemented at the plate and nozzle walls. To handle shock waves, a damping procedure using a dilatation-based shock detector and a second-order filter are used to remove Gibbs oscillations in the vicinity of shocks [21]. The radiation boundary conditions of Tam and Dong [23] are imposed to the radial and lateral boundaries of the computational domain. They are used in combination with sponge zones using grid stretching and Laplacian filtering to prevent significant spurious reflections. The method of Mohseni and Colonius [24] is applied to remove the singularity on the jet axis. Finally, the effective azimuthal resolution near the origin of the polar coordinates is reduced down to $2\pi/16$ to increase the time step of the simulation [25].

C. Computational Parameters

The numbers of points in the mesh grids used in the simulations are provided in Table 2. In the six simulations, they are equal to $N_r = 501$ and $N_\theta = 256$ in the radial and azimuthal directions, respectively. In the axial direction, the number of points N_z is equal to 2628 for jetfree, 1910 for jeth0, and 2950 for the jets impinging on perforated plates. The grids thus contain between 250 and 380 million points. They extend out to $r = 15r_0$ in the radial direction, and down to $z = 30r_0$ in the case with no hole and $z = 50r_0$ in the other cases in the axial direction. The variations of the radial mesh spacing Δr are presented in Fig. 2a. It is equal to $0.025r_0$ on the axis and progressively decreases down to $0.0072r_0$ in the shear layer at $r = r_0$. Farther from the jet axis, it then increases to reach $0.05r_0$ at

$r = 5r_0$, which leads to a Strouhal number $St = fD/u_e$ of 1.62 for an acoustic wave discretized with 5 points per wavelength, where f is the frequency. This value is significantly higher than the cutoff Strouhal number of about 0.2 reported in previous studies [2,3]. The variations of the axial mesh spacing Δz are plotted in Fig. 2b. The value of Δz is minimum and equal to $0.014r_0$ at the nozzle exit. For the free jet, it increases up to $0.03r_0$ at $z = 50r_0$. For the impinging jets, the axial mesh spacing grows up to a value of $0.022r_0$ at $z = 20r_0$, and then is constant. Downstream of $z \geq 25r_0$, it is reduced down to reach again $\Delta z = 0.014r_0$ at $z = 30r_0$, on the plate. For the plates with a hole, the axial mesh size increases downstream of the plate up to $\Delta z = 0.03r_0$ at $z = 50r_0$. The minimum and maximum values of the mesh spacings and the stretching rates in the radial and axial directions are the same as those in the simulations of jets at a Mach number of $M = 2$ of Pineau and Bogey [26,27]. The results in the present work are obtained for a simulation time of $1000r_0/u_e$. During the computations, the density, the velocity components, and the pressure are recorded along the jet axis at $r = 0$, along the lip line at $r = r_0$, on the surfaces at $r = 15r_0$, $z = -2r_0$, and $z = 0$, on the plate at $z = L$ and $z = L + e$, and at $z = 50r_0$. The sampling frequency enables the spectra to be computed up to $St = 12$. Density, velocities, and pressure at the azimuthal angles $\theta = 0, 90, 180$, and 270 degrees are also stored at half the sampling frequency mentioned above. In addition, the azimuthal Fourier coefficients of the density, pressure, and velocity fields are computed up to the mode $n_\theta = 4$ for $0 \leq z \leq 50r_0$ and $0 \leq r \leq 15r_0$. The spectra presented in Sec. III are calculated from these recordings, and they are averaged in the azimuthal direction when possible. On the whole, 200,000 time steps were performed for each jet, which consumed a total of 300,000 CPU hours.

III. Results

A. Snapshots of the Flow and Acoustic Fields

Fields of temperature and pressure fluctuations obtained inside and outside of the flow, respectively, are represented in Fig. 3. For the six jets, diamond patterns characteristic of shock cells are visible in the jets downstream of the nozzle exit. The cells are progressively weakened by the turbulent mixing for $z \geq 10r_0$. For jeth0, jeth1, and jeth2, in Figs. 3a–3c, a wall jet is created by the impingement of the flow on the plate. It is more apparent for the full plate than for the perforated plates. For these three jets, zones of high temperature are found in the impingement area, near the center of the plate for jeth0 or the hole edges for jeth1 and jeth2. For jeth3 and jeth4, the jets pass apparently fully through the plate, interacting more weakly with the hole edges.

In the pressure fields of the impinging jets in Figs. 3a–3e, circular waves centered on the impingement zone can be observed upstream. They are particularly visible for $z \leq 5r_0$. Their levels are highest for jeth0 and they seem to decrease as the hole diameter increases. For $z \geq 5r_0$, inclined wavefronts of strong amplitude are also seen to propagate in the downstream direction. They are typical of Mach wave radiation, as noticed in several previous simulations of free jets at Mach numbers higher than 2 [28–31]. These waves are produced

Table 2 Mesh parameters: numbers of points N_r , N_θ , and N_z in the radial, azimuthal, and axial directions, and total numbers of points

Jet	N_r	N_θ	N_z	$N_r \times N_\theta \times N_z$
jetfree	501	256	2628	3.4×10^8
jeth0	501	256	1910	2.5×10^8
jeth1, jeth2, jeth3, jeth4	501	256	2950	3.8×10^8

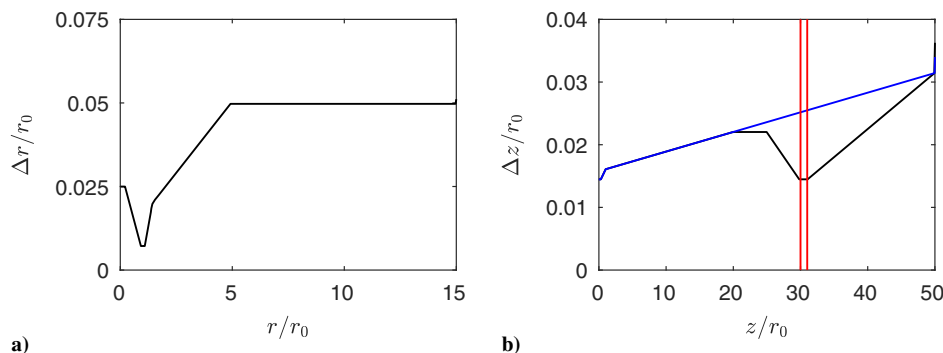


Fig. 2 Variations of a) radial and b) axial mesh spacings: — impinging jets, — free jet, and — positions of the upstream and downstream faces of the plate.

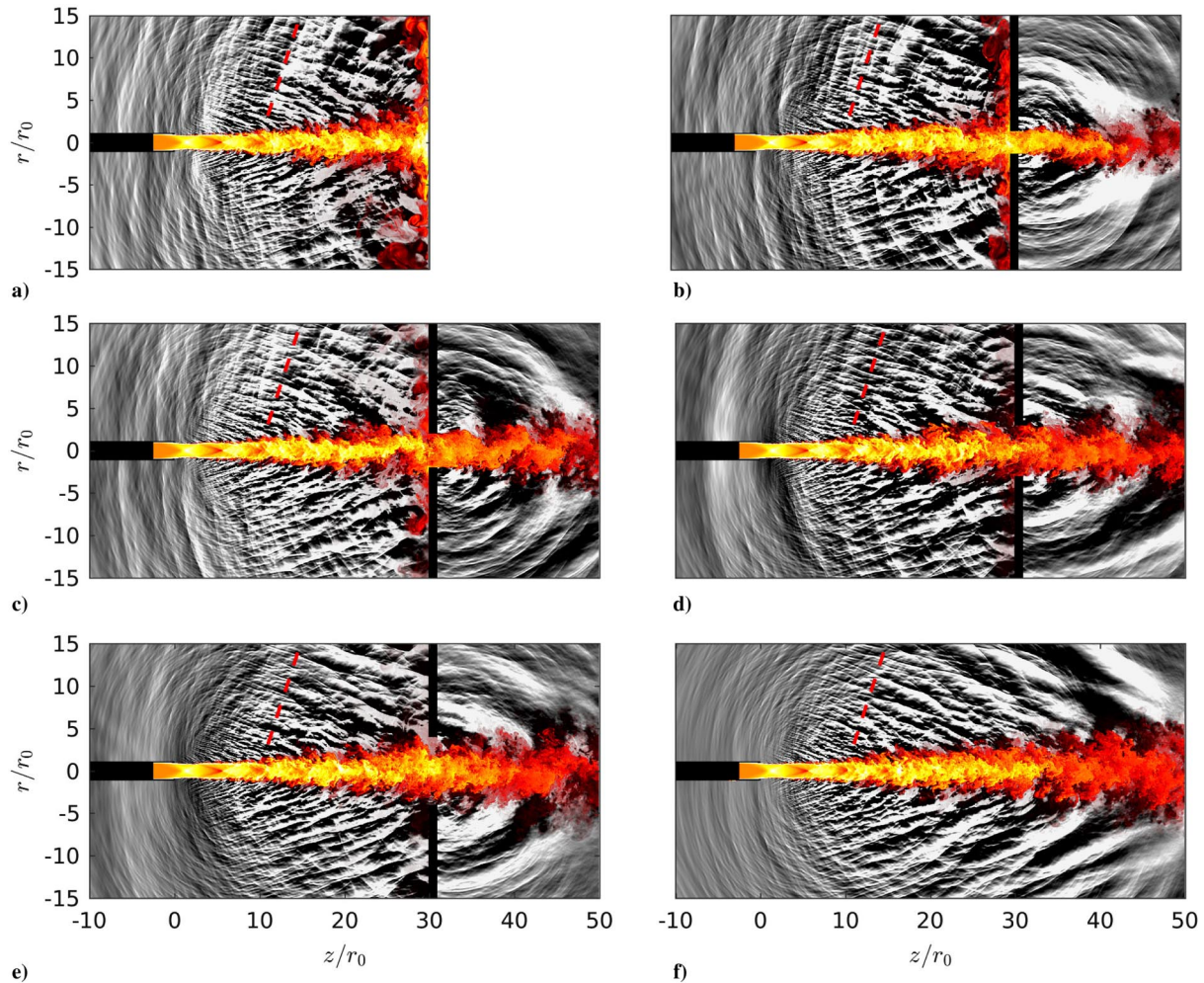


Fig. 3 Snapshots in the (z,r) plane of temperature fluctuations in the flow and of pressure fluctuations outside for a) jeth0, b) jeth1, c) jeth2, d) jeth3, e) jeth4, and f) jethfree. The color scales range from 0 to 780 K for temperature from red to white, and from -2000 to 2000 Pa for pressure from black to white. The red dashed line indicates the angle of $\alpha = 72^\circ$ with respect to the jet axis.

by the convection of turbulent coherent structures at a supersonic speed. The Mach angle α between the direction of propagation of the Mach waves and the jet axis can be approximated as

$$\alpha = \cos^{-1}\left(\frac{c_0}{u_c}\right) \quad (1)$$

where u_c is the mean convection velocity of the turbulent structures of the jet. This velocity has been estimated using frequency–wavenumber spectra computed in Sec. III.G and is close to $u_c = (2/3)u_e$ for all jets, yielding an angle α of 72° using Eq. (1). This value is consistent with the inclination of the Mach waves in Fig. 3. For the plates with a hole, in Figs. 3b–3e, the sound field downstream of the plate has no clear organization, even if acoustic waves can be seen to originate from the hole. In addition, no oblique wavefronts are present, suggesting that no Mach waves are generated for $z \geq L$. Finally, for the free jet, in Fig. 3f, Mach waves propagate in the downstream direction. Sound waves weaker than those generated by the impingement are also emitted in the upstream direction. They correspond to the broadband shock-associated noise (BBSAN) components produced by the interactions between the turbulent structures of the mixing layers and the shock cells [32,33].

B. Mean Flowfields

The variations of the centerline mean axial velocity obtained for the different jets are presented in Fig. 4a. Upstream of the plate, the profiles are very similar to each other down to $z = 28r_0$, indicating a

weak influence of the plate on the mean field. Significant oscillations are visible for $z \leq 18r_0$. They are linked to the presence of six shock cells, which are progressively damped by the turbulent mixing. The mean value of the length L_s of the first four cells is close to $4.6r_0$, in agreement with the experiments of Piantanida and Berterretche [14] and the simulations of Troyes et al. [3,34] and Langenais et al. [29]. To estimate the shock cell length, Tam and Tanna [35] proposed the following formula based on the work of Pack [36]

$$L_s = \frac{\pi D_j \beta}{\mu_1} \quad (2)$$

where $\beta = \sqrt{M_j^2 - 1}$ and $\mu_1 = 2.40483$ is the first zero of the zero-order Bessel function of the first kind. For the present jets, Eq. (2) yields a cell length $L_s = 6.4r_0$, which is larger than the values obtained in the simulations. This may be because Eq. (2) applies to weak shock cells [37] with $|M_e^2 - M_j^2| \leq 1$, whereas $|M_e^2 - M_j^2|$ is equal to 1.2 for the jets in the present work.

Downstream of the nozzle exit, the mean axial velocity oscillates around the exhaust velocity down to $z \approx 20r_0$. More precisely, the end of the potential core, defined arbitrarily by the position where the centerline axial velocity is equal to $0.9u_e$, is found at $z_c = 15.7r_0$. This potential core length can be compared with that predicted with the empirical formula proposed by Tam et al. [37]

$$\frac{z_c}{D_j} = 4.2 + 1.1M_j^2 + \left\{ \exp\left[-3.2\left(\frac{T_j}{T_0} - 1\right)\right] - 1 \right\} \quad (3)$$

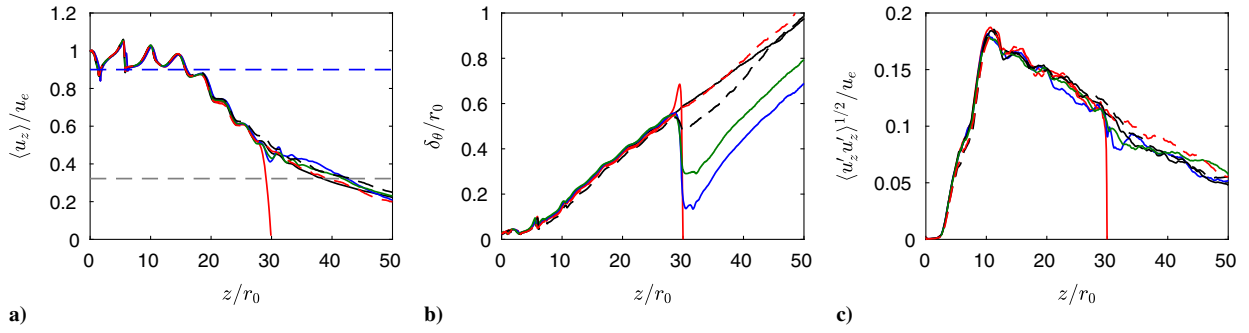


Fig. 4 Variations of a) the mean axial centerline velocity $\langle u_z \rangle / u_e$, b) the shear-layer momentum thickness δ_θ / r_0 , and c) the axial turbulence intensity $\langle u_z' u_z' \rangle^{1/2} / u_e$ at $r = r_0$ for — jetfree, — jeth0, - - - jeth1, — jeth2, - - - jeth3, and - - - jeth4; - - - $\langle u_z \rangle = 0.9u_j$ and - - - $\langle u_z \rangle = c_e$.

yielding $z_c = 23r_0$ for the present jets. The potential core is shorter in the LES, which can be explained by the fact that the constant values in relation (3) are based on measurements performed for a jet at a Mach number of 2.2 [38], lower than the Mach number of the present jets. Downstream of the potential core, for jeth0, the mean axial velocity falls down to zero at $z = 30r_0$ on the plate. For the other jets, for $z \geq 30r_0$, the velocity decreases gradually. The sonic core, in which the axial velocity is higher than c_e , closes around $z = 40r_0$. More precisely, its length is equal to $38.4r_0$ for jetfree, $42.4r_0$ for jeth1, $41.4r_0$ for jeth2, $42.6r_0$ for jeth3, and $39.5r_0$ for jeth4, revealing no clear link between the length of the sonic core and the hole diameter. More interestingly, the sonic core closes beyond the plate, in agreement with the simulations of Troyes et al. [3].

The shear-layer momentum thickness δ_θ obtained for the different jets is represented in Fig. 4b. Downstream of the nozzle, in all cases, it increases and reaches a value close to $0.56r_0$ at $z \approx 28r_0$, which compares well with the value of $0.65r_0$ obtained by Langenais et al. [29] at that position for a similar free jet. Oscillations due to the shock cells are also visible. For jetfree, for $z \geq 28r_0$, the shear-layer thickness continues to grow roughly linearly. For jeth0, it increases up to a maximum value of $0.69r_0$ at $z = 29.5r_0$ because of the wall jet spreading in the radial direction. For the other impinging jets, for $z \geq 28r_0$, it decreases down to a value of $0.14r_0$ for jeth1, $0.29r_0$ for jeth2, and $0.48r_0$ for jeth3 at $z = L$, due to the deflection of the flow along the plate, which increases with the hole diameter. Downstream of the plate, the shear-layer thickness grows again, at rates higher than that obtained for the free jet. For jeth3 and jeth4, despite much lower values of δ_θ at $z = L$, this leads to shear layers at $z = 50r_0$ slightly thicker than for jetfree.

The rms values of the axial velocity fluctuations at $r = r_0$ for the free and impinging jets are shown in Fig. 4c. From the nozzle exit down to $z = 2.5r_0$, they remain below 1%. Farther downstream, they grow sharply up to a peak value of $0.18u_e$ at $z \approx 11r_0$. The location and the amplitude of the peak are comparable to those in the simulation of a free jet at $M_e = 3.3$ by De Cacqueray et al. [28], for which a peak of axial turbulent intensity of $0.21u_e$ is found at $z = 12r_0$. For jeth0, for $z \geq 28r_0$, the amplitude of the fluctuations falls down to zero on the plate. For the other jets, the axial turbulent velocity decreases more slowly. For $z \geq 30r_0$, the turbulent levels are similar,

with differences around 2% of the jet exit velocity between the different cases.

For jeth0, jeth1, and jeth2, a high-speed wall jet is created by the impingement of the jet on the plate, as seen in the temperature snapshots of Sec. III.A. A wall jet has similarly been observed for supersonic jets impinging on an inclined plate in the experiments of Akamine et al. [39,40] for $M_j = 1.8$ and in the simulations of Nonomura et al. [41,42] for $M_j = 2$. In these studies, Mach waves were found to be emitted by the wall jet, due to the supersonic convection velocity of the jet turbulent structures. In the present work, to discuss the presence of such acoustic components, the profiles of the maximum mean radial Mach number $\langle M_r \rangle$ and of the turbulence intensity in the wall jets are depicted in Fig. 5 as a function of the distance to the jet axis for jeth0, jeth1, and jeth2. In Fig. 5a, for all jets, the Mach number is small close to the jet axis, then increases up to $r \approx 4r_0$, and finally decays as the wall jet spreads radially. The peak Mach number values are equal to 1.03 for jeth0, 0.76 for jeth1, and 0.59 for jeth2. The convection velocities $u_c \approx (2/3)\langle u_r \rangle$ of the coherent structures in the wall jets are thus subsonic, suggesting that no Mach waves are generated by the flow along the plate. Moreover, the Mach number $\langle M_r \rangle$ decreases as the hole diameter increases, indicating weaker wall jets for larger hole diameters. As for the maximum values of radial turbulent intensity, in Fig. 5b, they decrease with the radial distance in all cases. In addition, the amplitudes of the radial turbulent fluctuations are reduced as the hole is larger, as expected given the lower wall jet velocity.

The radial turbulence intensity profile of the free jet at $z = L$ and the corresponding pressure profiles obtained for all jets are plotted on Fig. 6. In Fig. 6a, the turbulence intensity is normalized by its maximum value $u_{z \max}^{\text{rms}}$. The radial position of the hole edges for the perforated plates are also plotted using blue dashed lines. The turbulence intensity for the free jet reaches a maximum value at $r = 0.74r_0$ and decreases down to about 10% of this value at $r = 5r_0$. Significant levels, approximately of 80 and 65% of the peak level, are found at $r = 1.33r_0$ and $r = 2r_0$, that is, at the positions of the edges of the two smallest holes. At the locations of the edges of the two largest holes, the levels are lower than for the previous cases and are equal to 40 and 25% of the peak level. The interactions between the flow vortical structures and the hole edges are thus expected to be

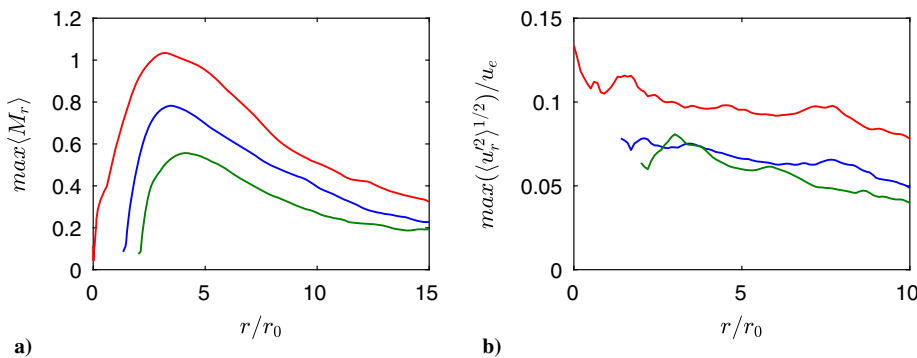


Fig. 5 Variations of maximum mean radial a) Mach number $\langle M_r \rangle$ and b) turbulence intensity $\langle u_r' \rangle^{1/2} / u_e$ in the wall jet for — jeth0, — jeth1, and — jeth2.

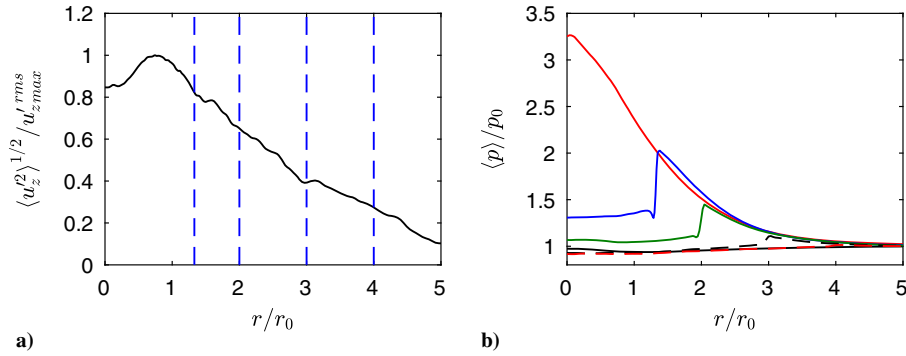


Fig. 6 Radial profiles at $z = L$ a) of the root-mean-squared axial velocity fluctuations normalized by their maximum $\langle u_z'^2 \rangle^{1/2} / u_{z,max}^{rms}$ for the free jet (--- position of the hole edges for the perforated plates), and b) of the mean pressure $\langle p \rangle / p_0$ for — jetfree, — jeth0, — jeth1, — jeth2, --- jeth3, and - - - jeth4.

stronger for jeth1 and jeth2 than for jeth3 and jeth4. As for the mean pressure on the plate, in Fig. 6b, it does not vary much with the radial distance and is close to the ambient pressure for the free jet. For jeth0, strong values of mean pressure are observed in the impingement area. The pressure is maximum at the center of the plate, with a value of $3.25p_0$, and decreases down to the ambient pressure at $r = 5r_0$. For the jets impinging on a perforated plate, for $r \leq h/2$, the mean pressure is lower than for jeth0 and tends toward that obtained for the free jet as the hole diameter increases. For jeth1 and jeth2, it is significantly higher than the ambient pressure, revealing a compression zone in the hole, which is not the case for jeth3 and jeth4. For $r \geq h/2$, the mean pressure is maximum on the hole edges and decays with the radial distance following closely the profile for jeth0.

C. Overall Sound Pressure Levels

The overall sound pressure levels (OASPLs) obtained at $r = 15r_0$ and at $z = 0$ are plotted in Figs. 7a and 7b, respectively. In Fig. 7a, for the free jet, the levels increase with the axial distance up to a maximum value of 160 dB at $z = 29r_0$. Farther downstream, they slowly decrease down to 155 dB at $z = 50r_0$. For jeth0, the sound levels also first increase, and then reach a peak value of 168 dB at $z = 28r_0$. The peak strongly emerges because of the presence of strong hydrodynamic pressure fluctuations of the wall jet in this near-plate region. Outside of this region, the sound levels for jeth0 are between 3 and 7 dB higher than those for the free jet. For the jets impinging on a plate with a hole, the levels upstream of the plate vary as those for jeth0. However, they decrease as the hole diameter increases. In comparison with the case with no hole, they are lower by 0.5–1 dB for jeth1 and jeth2, 2–3 dB for jeth3, and 2–4 dB for jeth4. This may be caused by the weaker interactions between the jet and the plate as the hole is larger. Downstream of the plate, the sound levels for the impinging jets are lower than for the free jet, which can be explained by the shielding of the jet acoustic radiation by the plate and by the deflection of a part of the jet flow along the plate. These hypotheses are also supported by the fact that the levels are the lowest for the smallest hole and that they grow with the hole diameter.

The sound levels obtained in the nozzle-exit plane at $z = 0$ are represented in Fig. 7b. For jetfree and jeth4, they slightly increase

with the radial distance, by 1.5 dB between $r = 2r_0$ and $r = 15r_0$, whereas for the other jets, they do not vary much. The levels are highest for jeth0, with a maximum value of 152.5 dB, and decrease as the hole diameter increases. Compared with jeth0, they are reduced by 0.9 dB for jeth1, 2.7 dB for jeth2, 3.9 dB for jeth3, 5.7 dB for jeth4, and 7.2 dB for jetfree.

D. Pressure Spectra

The acoustic spectra obtained in the LES are first compared with the measurements made at the MARTEL test bench. The sound pressure levels obtained at $z = -1.3r_0$ and $r = 10.5r_0$ for jeth1 and jeth2 are thus represented in Fig. 8 along with the corresponding experimental data. For both jets, the spectra compare well. They are broadband and exhibit bumps emerging by 1–5 dB from the broadband levels for Strouhal numbers between 0.02 and 0.4. For jeth1, in Fig. 8a, the results from the simulations and the experiments do not match very well for $St \leq 0.04$. However, a fairly good agreement is found for higher frequencies with a difference of less than 1 dB between $St = 0.04$ and 0.2. For jeth2, in Fig. 8b, one peak is found at $St = 0.065$ in the LES spectrum, whereas three peaks are present at $St = 0.035, 0.07, \text{ and } 0.11$ in the experimental spectrum. The LES peak frequency is similar to that of the strongest peak in the experiment. This frequency can be compared with the central frequency f_p of BBSAN estimated by the model of Harper-Bourne and Fisher [43]

$$f_p = \frac{u_c}{L_s(1 - M_c \cos \theta)} \quad (4)$$

where $M_c = u_c/c_0$ is the convection Mach number and θ is the angle between the jet direction and the far-field observation point. For $\theta = 180^\circ$, a Strouhal number of $St_p = 0.063$ is obtained using Eq. (4), which is close to the frequency of the dominant peaks in the spectra. Therefore, the peaks appear to be related to the BBSAN. For jeth2, the peak amplitude is 3 dB higher in the LES than in the experiments. The differences in the peak frequencies, amplitudes, and numbers in the experiments and the simulations may be due to the state of the mixing layer at the nozzle exit. Indeed, the turbulent intensity at the nozzle exit is equal to 1.5% in the LES, but is most

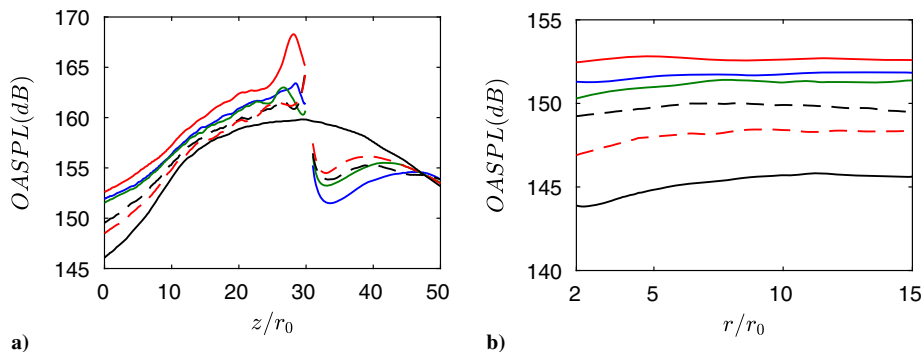


Fig. 7 Overall sound pressure levels at a) $r = 15r_0$ and b) $z = 0$ for — jetfree, — jeth0, — jeth1, — jeth2, --- jeth3, and - - - jeth4.

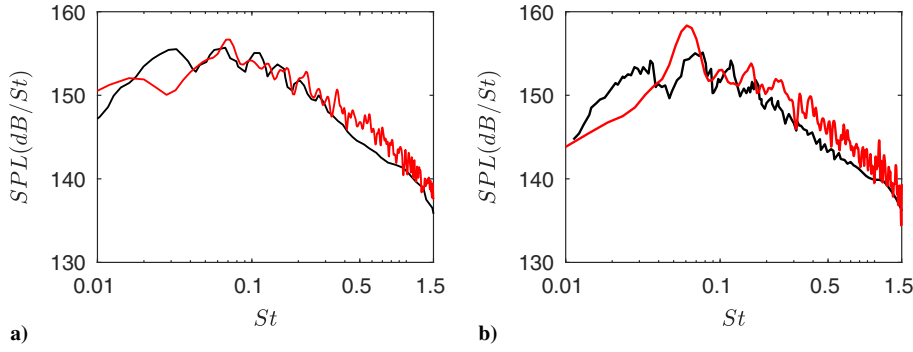


Fig. 8 Sound pressure levels at $z = -1.3r_0$ and $r = 10.5r_0$ for a) jeth1 and b) jeth2; — experiments [3], — present simulations.

probably higher in the experiments, which can affect the sound radiated by the jet [44].

The acoustic spectra estimated at three locations, namely, near the nozzle, near the plate, and downstream of the plate, are displayed in Fig. 9. The pressure spectra calculated at $z = 0$ and $r = 2r_0$ near the nozzle are shown in Fig. 9a. For the free jet, a peak centered on $St = 0.06$ appears. As discussed above, this peak is attributed to the BBSAN. For jeth0, the levels are approximately 12 dB higher than for the free jet, and the strongest components are found around $St = 0.04$. They may be generated by a feedback loop establishing between the nozzle and the plate, as will be discussed later. However, the absence of strongly emerging tones implies that such a feedback may be weak. For the plates with a hole, the sound levels decrease as the hole diameter increases. More precisely, for jeth1 and jeth2, compared with the no-hole case, the acoustic levels are reduced by about 3 dB for jeth1 and 4 dB for jeth2 for $St \geq 0.1$. For jeth3, a noise reduction of 4 dB is observed for all frequencies with respect to jeth2. Finally, for jeth4, for $St \leq 0.2$, the pressure levels decrease by approximately 2 dB relative to jeth3. This diminution of the upstream noise suggests that the interactions between the jet and the hole edges are weaker for larger holes. This result is consistent with the radial profiles of the mean pressure at $z = L$ in Fig. 6b, revealing a compression zone in the hole of the plate for jeth1 and jeth2 but not for jeth3 and jeth4.

The acoustic spectra computed at $z = 20r_0$ and $r = 15r_0$, in the direction of propagation of the Mach waves, are represented in Fig. 9b. The spectra display a similar shape, reaching a peak at a Strouhal number between 0.11 and 0.15. For $St > 0.5$, they are almost superimposed. At lower frequencies, the levels are highest for jeth0, decrease as the hole widens, and are lowest for the free jet. The differences between the free jet and the impinging jets are larger as the frequency decreases. In comparison with those for the free jet, for $St < 0.2$, the levels increase by at most 14 dB for jeth0, 12 dB for jeth1 and jeth2, and 10 dB for jeth3 and jeth4. The strengthening of the acoustic waves at low frequencies can be attributed to the jet impingement on the plate.

Finally, the sound pressure levels obtained downstream of the plate at $z = 40r_0$ and $r = 15r_0$ are plotted in Fig. 9c. The spectra are all centered on a peak at Strouhal numbers around $St \approx 0.09$, and for

$St \geq 0.5$, the spectra almost overlap. For lower Strouhal numbers, they are minimal for jeth1 and increase with the hole diameter. Compared with those for jeth1, the levels increase by roughly 2 dB for jeth2, 3 dB for jeth3, 4 dB for jeth4, and 5 dB for the free jet. Indeed, for the impinging jets, the Mach waves generated in the jet shear layers are shielded by the plate. A significant part of the flow is also diverted in the wall jet, leading to a weaker noise radiation of the jets downstream of the plate.

To highlight the azimuthal structure of the acoustic waves radiated in the upstream direction, the contributions of the first four azimuthal modes to the pressure spectra at $z = 0$ and $r = 2r_0$ are shown in Fig. 10. Similar trends are found for all jets. For $St \leq 0.1$, where the acoustic levels are highest and reach a maximum value at $St = 0.04$, the axisymmetric mode $n_\theta = 0$ is dominant. For higher frequencies, the contributions of modes $n_\theta \geq 1$ are significant and become similar to that of the mode $n_\theta = 0$ as the Strouhal number increases. Therefore, the azimuthal structure of the upstream acoustic field is not significantly affected by the jet impingement on the plate. However, small differences can be noted between the jets. For instance, the spectra for the mode $n_\theta = 0$ exhibit a hump at $St \approx 0.09$ for jeth2, jeth3 and jeth4 in Figs. 10c–10e, but not for the other jets. For jeth4 and jethfree in Fig. 10e and 10f, peaks are also observed around $St \approx 0.15$ for $n_\theta = 3$ and 4. For lower modes, the peaks may be related to feedback loops establishing between the nozzle and the plate. However, no reason was found to explain the differences in the peak levels, prominence, and azimuthal order between the different jets.

E. Spatial Fourier Decomposition of the Pressure Fields

A two-dimensional spatial Fourier transform has been applied to the pressure fields of the jets in the radial and axial directions using the method developed by Nonomura et al. [45] for free jets at an exit Mach number of 2. For the jets impinging on a perforated plate, the results are similar. Therefore, only those for jeth1 are presented. The regions over which the Fourier transform is performed are represented in Fig. 11 for jethfree, jeth0, and jeth1. In the three cases, they extend axially from $z = 5r_0$ down to $z = 25r_0$ and radially from $r = 5r_0$ out to $r = 15r_0$. This area is chosen far enough from the jet so that the pressure fluctuations are purely acoustic. In all cases, Mach waves are seen to propagate downstream. For jethfree, in Fig. 11a,

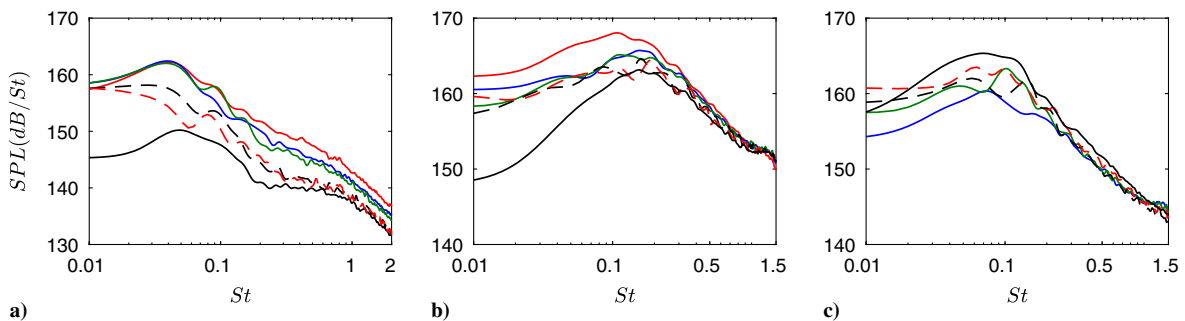


Fig. 9 Sound pressure levels (SPLs) at a) $z = 0$ and $r = 2r_0$, b) $z = 20r_0$ and $r = 15r_0$, and c) $z = 40r_0$ and $r = 15r_0$ as a function of the Strouhal number St : — jeth0, — jeth1, — jeth2, - - - jeth3, - - - jeth4, and — jethfree.

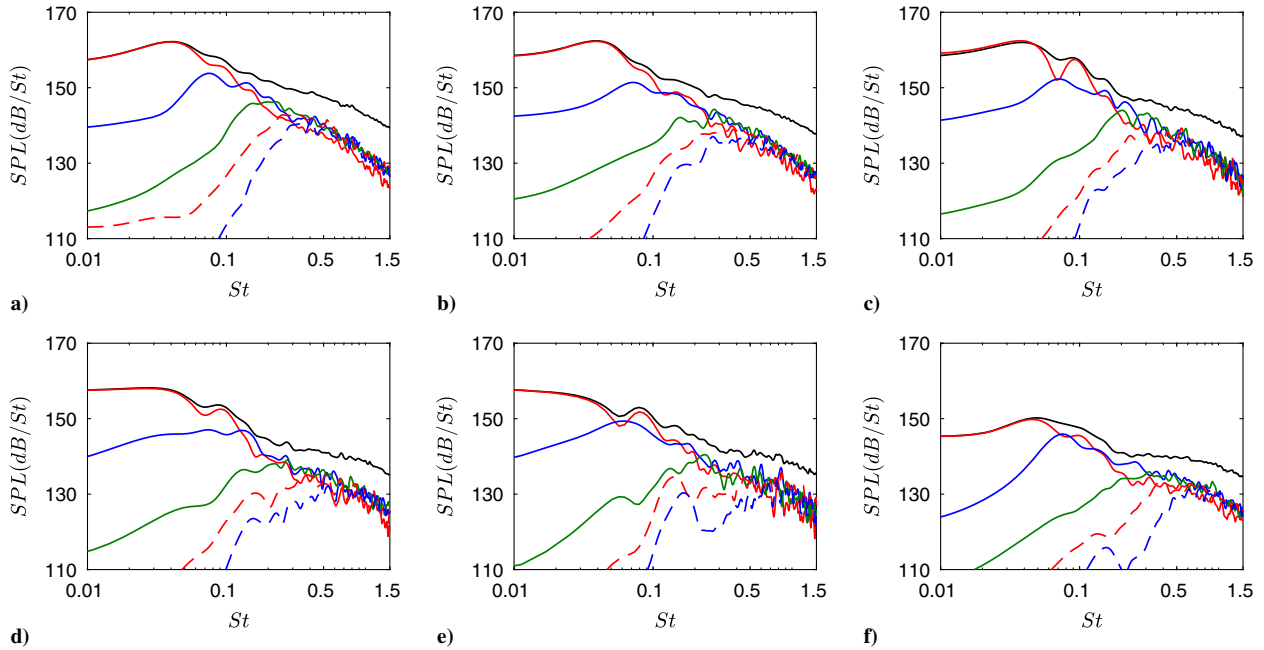


Fig. 10 Sound pressure spectra at $z = 0$ and $r = 2r_0$ for a) jeth0, b) jeth1, c) jeth2, d) jeth3, e) jeth4, and f) jefree: — full spectra, and for modes $n_\theta = 0$, $n_\theta = 1$, $n_\theta = 2$, $n_\theta = 3$, and $n_\theta = 4$.

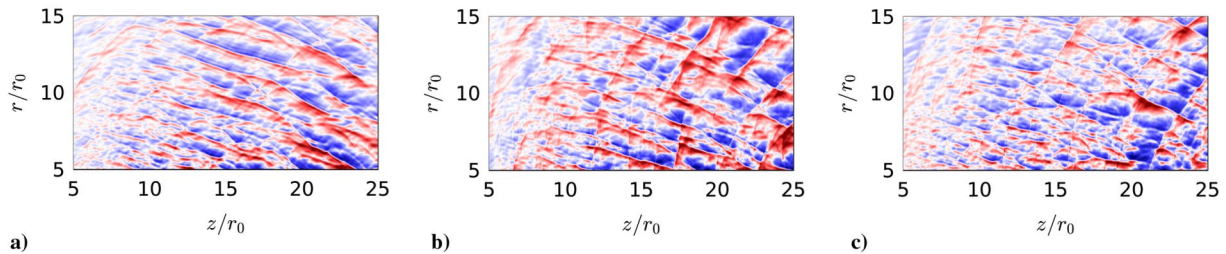


Fig. 11 Pressure fluctuations for a) jefree, b) jeth0, and c) jeth1. The color scale levels vary within $\pm 0.1p_0$, from blue to red.

upstream-propagating waves of very weak amplitude are observed for $z \leq 10r_0$. For jeth0 and jeth1, in Figs. 11b and 11c, upstream-traveling pressure waves with circular fronts are also noticeable throughout the whole domain, especially between $z = 20r_0$ and $z = 25r_0$. They are less marked for jeth1 with a hole in the plate, suggesting that the waves are produced by the jet impingement on the plate.

The spatial Fourier decomposition is performed at each recorded time and for the four (z, r) planes mentioned in Sec. II.C. The Fourier transforms of the pressure signals are then averaged over the four planes and over time. The amplitudes thus obtained are presented in Fig. 12 as a function of the radial and axial wavenumbers k_r and k_z , for $k_r \geq 0$. For the free jet, in Fig. 12a, a lobe is observed for the positive axial wavenumbers k_z . It can be associated with downstream-propagating waves. The lobe is well aligned with the direction of propagation of the Mach waves, showing that the latter ones are the main

acoustic components in the pressure field. A similar lobe can be seen for the impinging jets in Figs. 12b and 12c. However, a lobe is also found for $k_z \leq 0$, revealing the presence of upstream-propagating waves. The orientation of the lobe is compared with the direction of propagation of reflected Mach waves, assuming a specular reflection on the plate. It does not agree with this direction, implying that the reflected Mach waves have negligible contributions in the acoustic region considered. For both impinging jets, the lobe is approximately aligned with the direction $\alpha = 150^\circ$. Thus, the directivity of the upstream-travelling pressure waves is weakly affected by the presence of the hole in the plate. The amplitude fields also provide information on the frequency content of the sound waves, since in the wavenumber plane (k_z, k_r) , the distance of a point to the origin is proportional to the frequency. For the impinging jets in Figs. 12b and 12c, the lobe related to upstream-propagating waves does not extend as far from the origin

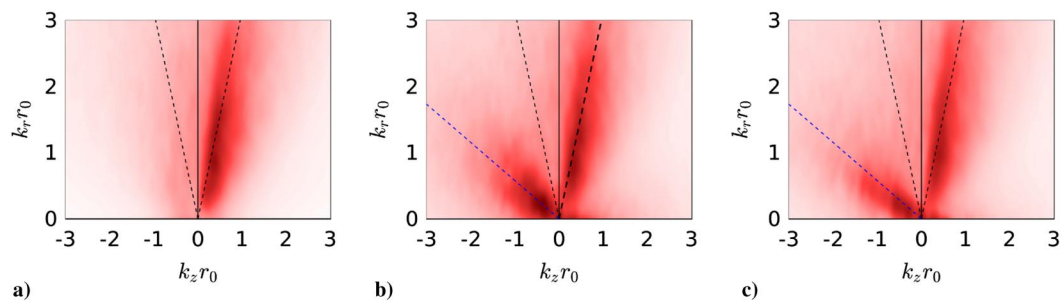


Fig. 12 Two-dimensional wavenumber spectra as a function of (k_r, k_z) for a) jefree, b) jeth0, and c) jeth1; — — propagation directions of $\alpha = 72^\circ$ and 108° of the incident and reflected Mach waves, --- direction $\alpha = 150^\circ$. The color scale levels spread over 35 dB from white to red.

as that of the downstream-propagating waves, indicating that the upstream noise components have lower frequencies than the downstream components. This result is consistent with the sound spectra in Fig. 9. This provides further evidence that the main upstream noise components are not generated by the reflections of the downstream noise on the plate. The lobe associated with the upstream sound waves is also less extended for jeth1 than for jeth0, which implies that the presence of the hole in the plate reduces the amplitude of the high-frequency upstream components. Moreover, the levels for the negative wavenumbers k_z are lower for jeth1 than for jeth0, suggesting that no significant additional sound sources are created by the interactions between the flow and the hole edges. In other words, the noise in the upstream direction is mainly produced by the impingement of turbulent structures on the plate.

The characteristics of the pressure waves can be investigated separately according to their propagation direction using the two-dimensional wavenumber spectra. To evaluate the intensities of the waves, the sound powers W_d and W_u associated with the downstream and the upstream-propagating waves, respectively, are computed as

$$W_d = \frac{1}{\rho_0 c_0} \iint_{k_z > 0} |\tilde{p}(k_z, k_r)|^2 dk_z dk_r \quad (5)$$

$$W_u = \frac{1}{\rho_0 c_0} \iint_{k_z < 0} |\tilde{p}(k_z, k_r)|^2 dk_z dk_r \quad (6)$$

where \tilde{p} is the Fourier transform in the z and r directions of the pressure fluctuations in the areas shown in Fig. 11 and ρ_0 is the ambient density. The variations of W_d and W_u with the hole diameter are presented in Fig. 13. They are normalized by the values W_d^f and W_u^f obtained for the free jet. For the downstream-propagating waves, in Fig. 13a, the sound power does not vary much with the hole diameter and remains close to that of the free jet. Therefore, the jet impingement on the plate has very limited effects on the downstream acoustic levels. In particular, the generation of Mach waves does not seem to be affected by the plate. For the upstream-propagating waves, in Fig. 13b, the power is close to that for the free jet for jeth4 with the largest hole, and increases as the

hole diameter decreases. In that case, the noise radiated upstream is significantly enhanced by the jet impingement on the plate. Notably, for $h \leq 2D$, the power of the upstream sound radiation is more than two times higher than for the free jet.

F. Two-Dimensional Spatial Correlations

To visualize the different noise components, two-dimensional spatial correlations of the jet pressure fields have been calculated in a section (z, r) . The fluctuating pressure p' at a reference point (z_1, r_1) at time t is correlated with the pressure fluctuations in the plane (z, r) at time $t + \delta t$, giving the dimensionless coefficient \mathcal{R} :

$$\mathcal{R}(r, z, \delta t) = \frac{\langle p'(r_1, z_1, t) p'(r, z, t + \delta t) \rangle}{\langle p'^2(r_1, z_1, t) \rangle^{1/2} \langle p'^2(r, z, t) \rangle^{1/2}} \quad (7)$$

where δt is the time delay between the signals and $\langle \cdot \rangle$ denotes time averaging. In this manner, the shapes and the time variations of the waves correlated with the pressure fluctuations at the reference point are revealed. The correlation coefficient \mathcal{R} has been evaluated for all jets at different reference points to study the sound radiation upstream and downstream of the plate. The results of the impinging jets are similar to each other. Therefore, only those for jeth2 are shown.

1. Upstream of the Plate

The correlations are first calculated for a reference point near the nozzle at $z_1 = 0$ and $r_1 = 2r_0$, in order to first focus on the upstream acoustic radiation. The results obtained for jeth2 are presented in Fig. 14 for time delays $\delta t = -100r_0/u_e$, $-50r_0/u_e$, and 0 . For $\delta t = -100r_0/u_e$, in Fig. 14a, three curved fronts of positive correlations are observed, located around $z = 0$, $z = 10r_0$, and $z = 20r_0$ for $r \approx 0$. They are separated by a distance close to the wavelength $\lambda = 10.2r_0$ corresponding to the Strouhal number $St = 0.04$ of the strongest noise components near the nozzle. The levels of correlations are highest for the front at $z \approx 20r_0$. In the vicinity of the jet axis, for $r \leq 5r_0$, the front is roughly aligned with a circle centered on the hole edge at $z = L$ and $r = h/2$, suggesting that the main upstream noise components are generated on the plate near the hole edge.

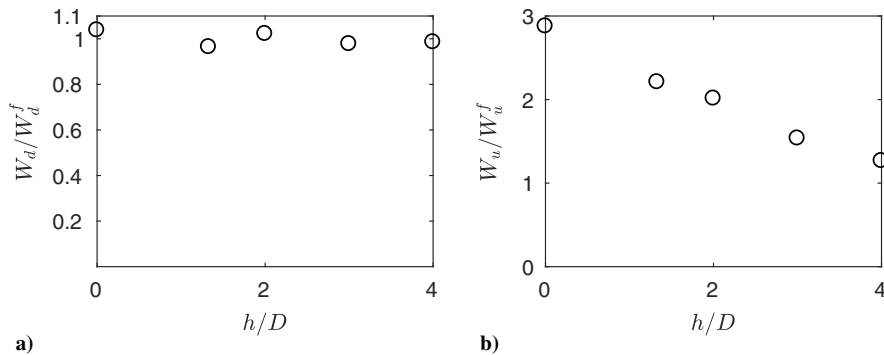


Fig. 13 Variations with the hole diameter of the sound powers a) of the downstream-propagating waves W_d and b) of the upstream-propagating waves W_u , normalized by the values W_d^f and W_u^f obtained for jethree.

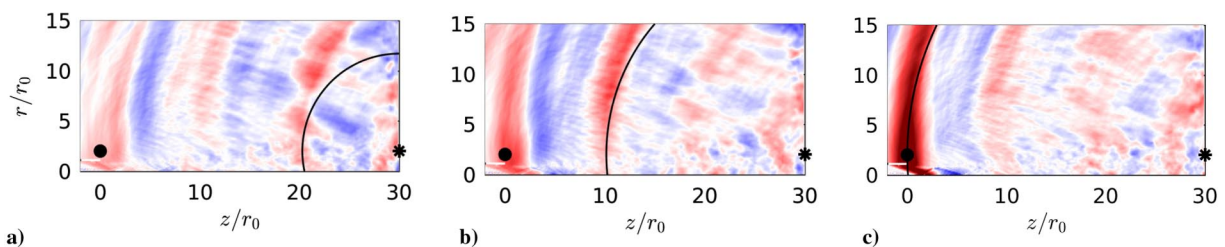


Fig. 14 Correlations \mathcal{R} of $p'(r = 2r_0, z = 0, t)$ with $p'(r, z, t + \delta t)$ for a) $\delta t = -100r_0/u_e$, b) $\delta t = -50r_0/u_e$ and c) $\delta t = 0$ for jeth2; — circle centered on * at $(z = L, r = h/2)$. The color scale varies within ± 0.5 , from blue to red.

Farther from the axis, the agreement between the correlation front and the circle is poorer, which may be due to the effects of the high-speed wall jet on the propagation of the sound waves produced on the wall. For $\delta t = -50r_0/u_e$, in Fig. 14b, the correlation levels are higher than previously. The wavefronts propagate to the reference point over a distance of about $10r_0$, which is consistent with the distance $c_0 \times 50r_0/u_e$ traveled by a sound wave during the time interval between two correlation snapshots. For $\delta t = 0$, in Fig. 14c, the correlation coefficient is equal to 1 on the reference point, as expected. Strong levels of correlations are visible outside but also inside of the jet flow in the vicinity of the nozzle exit, highlighting a link with the guided jet modes, which will be investigated later in Sec. III.G.

The correlation levels are then computed for a reference point near the plate at $z_1 = 20r_0$ and $r_1 = 15r_0$ with the aim of examining the acoustic waves propagating in the radial direction. The results for jeth2 are shown in Fig. 15 for $\delta t = -40r_0/u_e$, $-20r_0/u_e$, and 0. For $\delta t = -40r_0/u_e$, in Fig. 15a, two areas of significant correlations appear. The first one is straight and is aligned with the direction $\alpha = 72^\circ$ of the incident Mach waves observed in the pressure snapshots of Fig. 3. The second one is curved and seems to originate from the hole edge. Compared with an arc centered on the edge, however, it is ovalized due to the effects of the wall jet on the propagation of the acoustic waves, as discussed previously. In particular, no correlation front parallel to possible reflected Mach waves can be seen, indicating that the contributions of these reflections to the radiated sound are negligible at the reference point. Therefore, the acoustic radiation consists of two main components, namely, the incident Mach waves and the waves generated at the impingement point. For

$\delta t = -20r_0/u_e$, in Fig. 15b, the two contributions propagate to the reference point. Finally, for $\delta t = 0$, in Fig. 15c, they reach that point, causing a correlation level of 1.

2. Downstream of the Plate

Two-dimensional spatial correlations are also estimated for a point at $z_1 = 40r_0$ and $r_1 = 15r_0$ in order to visualize the noise radiation in the downstream direction. The correlation coefficients obtained for the free jet are given in Fig. 16 for the time delays $\delta t = -75r_0/u_e$, $-45r_0/u_e$, and $-15r_0/u_e$. For $\delta t = -75r_0/u_e$, in Fig. 16a, a spot of strong correlations is found in the jet shear layer at $z \approx 30r_0$. An inclined front of high positive correlations also emerges outside the flow at this position. These features indicate the generation of Mach waves by flow structures convected at a supersonic speed. Similar results were obtained in previous studies using conditional averages for temporal jets at Mach numbers of 2 and 3 [31,46], for instance. Later, for $\delta t = -45r_0/u_e$, in Fig. 16b, the pressure wave leaves the flow, creating a straight band of strong correlations propagating at an angle of $\alpha = 58^\circ$ with respect to the jet axis. This angle is lower than that of the Mach waves $\alpha = 72^\circ$ observed for $z < 30r_0$, which can be explained by the decrease of the convection velocity of the jet vortical structures with the axial distance. Finally, for $\delta t = -15r_0/u_e$, in Fig. 16c, the wave propagates to the reference point.

The correlations evaluated for a reference point at $z_1 = 40r_0$ and $r_1 = 15r_0$ for jeth2 are presented in Fig. 17 for the same time delays as for the free jet in order to give insight into the acoustic radiation downstream of the perforated plate. For $\delta t = -75r_0/u_e$, in Fig. 17a, significant correlation levels are noted near the hole in the plate,

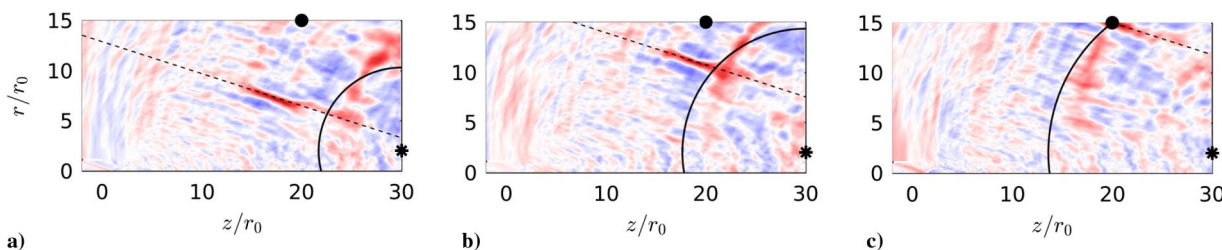


Fig. 15 Correlations \mathcal{R} of $p'(r = 15r_0, z = 20r_0, t)$ with $p'(r, z, t + \delta t)$ for a) $\delta t = -40r_0/u_e$, b) $\delta t = -20r_0/u_e$, and c) $\delta t = 0$ for jeth2; — circle centered on * at $(z = L, r = h/2)$ and - - - wavefront for a propagation at an angle of $\alpha = 72^\circ$ with respect to the jet axis. The color scale varies within ± 0.5 , from blue to red.

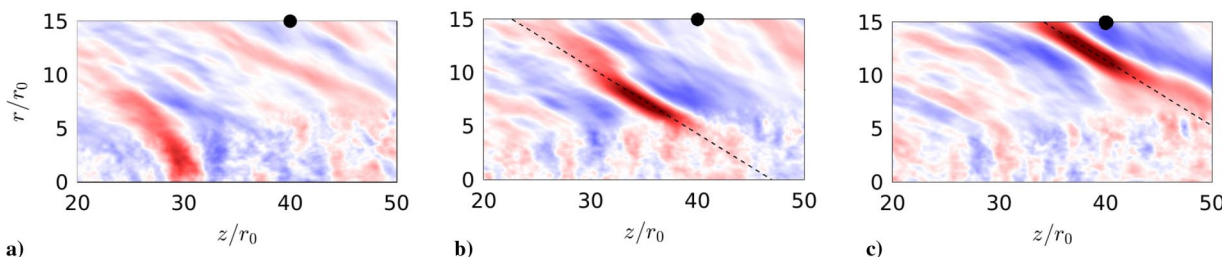


Fig. 16 Correlations \mathcal{R} of $p'(r = 15r_0, z = 40r_0, t)$ with $p'(r, z, t + \delta t)$ for a) $\delta t = -75r_0/u_e$, b) $\delta t = -45r_0/u_e$, and c) $\delta t = -15r_0/u_e$ for jethfree. The dashed line indicates the wavefront for a propagation at an angle of $\alpha = 58^\circ$ with respect to the jet axis. The color scale varies within ± 0.5 , from blue to red.

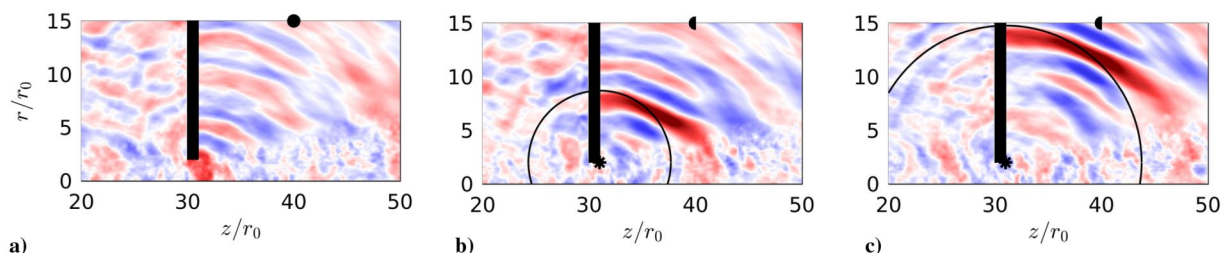


Fig. 17 Correlations \mathcal{R} of $p'(r = 15r_0, z = 40r_0, t)$ with $p'(r, z, t + \delta t)$ for a) $\delta t = -75r_0/u_e$, b) $\delta t = -45r_0/u_e$, and c) $\delta t = -15r_0/u_e$ for jeth2, — circle centered on * at $(z = L + e, r = h/2)$. The color scale varies within ± 0.5 , from blue to red.

revealing interactions between the jet flow and the plate. No clear organization of the correlation field is observed upstream of the plate, whereas fronts of positive correlations centered on the hole are seen downstream of the plate. For $\delta t = -45r_0/u_e$, in Fig. 17b, a front of strong correlations is noticed downstream of the plate. Contrary to the wavefront observed at the same time delay for the free jet in Fig. 16b, it is curved, indicating that the dominant sound waves downstream of the plate for jeth2 are not Mach waves. More precisely, the correlation front is approximately aligned with a circle centered on the hole edge at $z = L + e$ and $r = h/2$, except in the downstream direction, most likely due to the effects of the jet flow on the acoustic wave propagation. This suggests that the sound radiation results from the interactions between the jet turbulent structures and the plate. For $\delta t = -15r_0/u_e$, in Fig. 17c, as for the free jet, the wave travels to the reference point.

G. Frequency–Wavenumber Spectra

The guided jet waves play an important role in the generation of tones in the near-nozzle pressure fields of free and impinging high-speed jets [6,11,47,48]. These waves propagate mostly in the jet column, are organized according to their radial and azimuthal structures, and are defined by specific dispersion relations [49]. Their characteristics have been described for free jets at Mach numbers varying from 0.5 to 2 in various studies [19,47,50,51]. For impinging jets at Mach numbers lower than 2, they were shown to form the upstream part of the feedback loops establishing between the nozzle and the plate [11,12]. For impinging jets at Mach numbers around 3, the existence of such feedback loops is less obvious. To discuss this issue, a space–time Fourier transform has been applied to the pressure fluctuations in the potential core of the present jets between $z = 0$ and $z = z_c$ at $r = 0$. The results are similar for all the impinging jets. Therefore, only those for jeth2 and jeth1 are presented in what follows. The frequency–wavenumber spectra obtained are plotted in Fig. 18. Only the negative wavenumbers part of the spectra are represented to study the upstream-propagating waves likely to close possible feedback loops. For comparison, the dispersion relations of the guided jet modes computed for a hot jet at $M_e = 3.1$ using a vortex-sheet model [49] for the axisymmetric mode $n_\theta = 0$ are also displayed.

For the free jet, in Fig. 18a, two bands of high intensity can be seen in the frequency–wavenumber spectrum. They can be related to two radial modes of the guided jet waves. However, they do not agree very well with the dispersion curves of the guided jet modes predicted by the vortex-sheet model. This may be explained by the assumptions of flow motions of weak amplitudes and of an infinitely thin shear layer in the model, which are not valid for the present jets. For jeth2, in Fig. 18b, the levels are higher than for jeth1 in Fig. 18a. They are strongest in two spots located near the sonic line $k = -\omega/c_0$ around $St = 0.04$ and $St = 0.08$. The spots are found at frequencies close to those of the humps in the near-nozzle pressure spectra for $n_\theta = 0$ for jeth2, indicated by red triangles arbitrarily positioned at $k = 0$. They intersect the branches of the first and second radial modes of the guided jet waves at points where the waves have negative group

velocities. The humps in the near-nozzle spectra for the impinging jets may thus be generated by feedback loops establishing between the nozzle and the plate closed by upstream-propagating guided jet waves. However, unlike the case of impinging jets generating intense tones [12,13], the spots of high energy in the frequency–wavenumber spectrum do not extend over all wavenumbers. Therefore, the feedback phenomenon in the present jets is probably weak, which may be due, at least in part, to the large nozzle-to-plate distance.

In Fig. 18, the dispersion curves associated with the upstream-propagating guided jet waves are all located under the line $k = -\omega/c_0$, indicating a subsonic phase velocity. In this way, these waves belong to the family of the subsonic instability waves described by Tam and Hu [49]. These authors also identified two other kinds of instability waves produced in high-speed jets, namely, the Kelvin–Helmholtz and the supersonic instability waves. The Kelvin–Helmholtz waves are related to the coherent structures in the mixing layer. As the subsonic instability waves, they can be found in both subsonic and supersonic jets, whereas the supersonic instability waves are present only for supersonic jets for which

$$u_j > c_j + c_0 \quad (8)$$

This condition is satisfied for the present jets, indicating that the supersonic instability waves can exist. To verify this, the frequency–wavenumber spectra calculated for $n_\theta = 0$ at $r = 0$ and $r = r_0$ for the free jet are presented in Fig. 19 for both positive and negative wavenumbers. A snapshot of the pressure fluctuations in the sound field of the free jet is also displayed in Fig. 20, in which two kinds of waves with different angles appear, as was observed by Nonomura et al. [45] for jets at $M = 2$. In the frequency–wavenumber spectrum computed at $r = r_0$, in Fig. 19a, spots of high energy emerge for $k \geq 0$. They are close to the line $k = \omega/u_c$ with $u_c = (2/3)u_e$, and can therefore be attributed to Kelvin–Helmholtz waves. Due to their supersonic convection speed, the direction of propagation of the waves radiated by these instabilities can be estimated by

$$\alpha = \cos^{-1}\left(\frac{c_0}{v_\varphi}\right) \quad (9)$$

where $v_\varphi = \omega/k$ is the instability phase velocity, yielding $\alpha = 72^\circ$ for $v_\varphi = u_c$. In the pressure field in Fig. 8, marked wavefronts perpendicular to this direction are visible, indicating the radiation of Mach waves by Kelvin–Helmholtz instabilities outside of the jet flow.

In the spectrum obtained on the jet axis, in Fig. 19b, two elongated bands of high intensity are clearly found for negative wavenumbers, as mentioned previously. For positive wavenumbers near the line $k = \omega/u_c$, the levels are approximately 6 dB lower than those obtained for $r = r_0$, which is explained by the fact that the fluctuations of pressure associated with the Kelvin–Helmholtz waves are confined to the region very near the shear layer, and are very low on the jet centerline [49]. A large band of strong intensity is visible at the

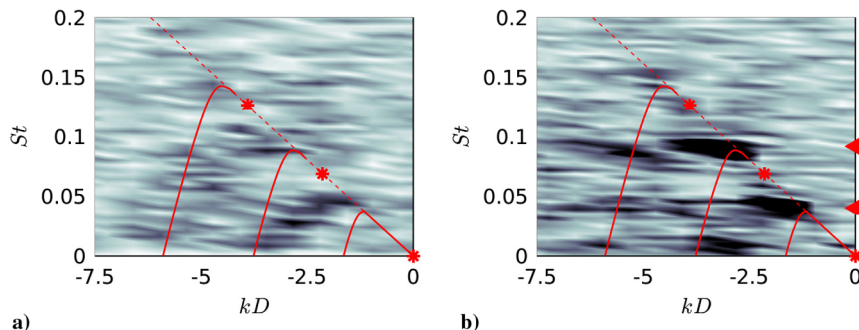


Fig. 18 Frequency–wavenumber spectra of the pressure fluctuations at $r = 0$ for a) jeth1 and b) jeth2 for $n_\theta = 0$; --- $k = -\omega/c_0$, — dispersion curves, and * lower limits of the guided jet modes for a vortex-sheet model and ◀ LES peak frequencies in the pressure spectra for jeth2. The grayscale levels spread over 25 dB.

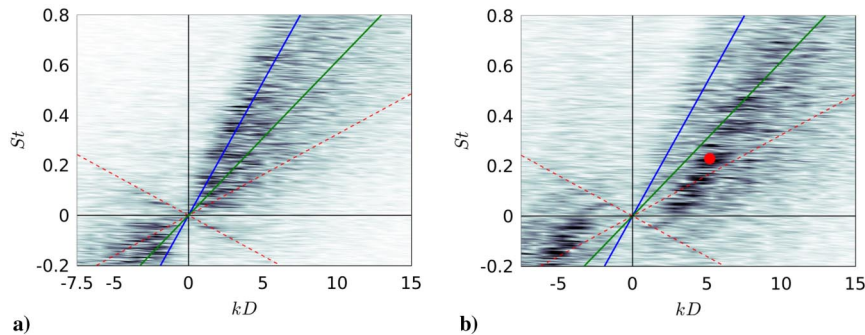


Fig. 19 Frequency–wavenumber spectra of the pressure fluctuations at a) $r = r_0$ and b) $r = 0$ for jetfree for $n_0 = 0$; $---$ $k = \pm\omega/c_0$, $---$ $k = \omega/u_c$ with $u_c = (2/3)u_e$, $---$ $k = \omega/v_\phi$ with $v_\phi/c_0 = u_e/(c_e + c_0)$, and \bullet maximum energy level of the supersonic waves. The grayscale levels spread over 25 dB. They are higher by 4.5 dB for (b) than for (a).

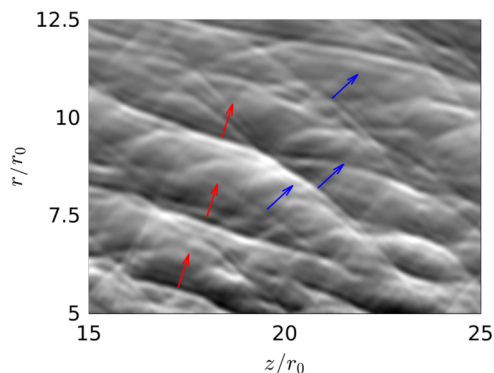


Fig. 20 Snapshots of pressure fluctuations for jetfree. The color scale ranges from $-10,000$ to $10,000$ Pa from black to white. The red and blue arrows indicate the directions of propagation of $\alpha = 72^\circ$ and 43° , respectively.

right of the line $k = \omega/u_c$. This band is the continuation of the first band of the guided jet waves in the negative wavenumber part of the spectrum. As the frequency increases, it crosses the line $k = \omega/c_0$, leading to subsonic and supersonic instability waves at low and high Strouhal numbers, respectively. The position of the peak level of the supersonic waves in the spectrum is indicated by a red dot. The phase velocity at this point is equal to $v_\phi = 1.36c_0$, giving an angle of propagation of 43° using Eq. (9). In the pressure snapshot of Fig. 8, waves less inclined and less intense than the Mach waves due to Kelvin–Helmholtz waves are seen to propagate in a direction consistent with this angle. This result suggests that these waves propagating outside the jet are related to the supersonic instability waves.

More specific work would be necessary to better characterize the supersonic instability waves and their contributions to the acoustic field. It can be, however, noted that, according to both experimental [52] and theoretical [49,53] studies, the most likely observed phase velocity of the supersonic instability waves is expected to be given by

$$\frac{v_\phi}{c_0} = \frac{u_e}{c_e + c_0} \quad (10)$$

This phase velocity is represented by the green line in Fig. 19b. The high-intensity components associated with supersonic instability waves in the spectrum are close to this line for $St \geq 0.4$. They are below the line for lower frequencies, where the peak level of the supersonic waves is in particular found, leading to less inclined wavefronts in the jet near field.

IV. Conclusions

In this paper, the sound radiation of rocket jets impinging on a plate with and without a hole for different hole diameters h has been studied using highly resolved large-eddy simulations. The effects of the plate and of the hole on the flow and acoustic fields have been

examined by comparing with the results obtained for the corresponding free jet. For all impinging jets, it is found, using two-dimensional spatial correlations and spatial Fourier transforms, that the upstream and radial acoustic radiations are mainly produced by the impingement of the turbulent structures of the jet flow on the plate and that the sound reflections on the plate have negligible contributions near the jet nozzle. The sound waves upstream of the plate are weaker as the hole widens. In particular, compared with the full-plate case, for a hole diameter $h \leq 2D$, the near-nozzle pressure levels are reduced at high frequencies only, whereas for $h \geq 3D$, they are lower for all frequencies. This is due to less intense interactions between the turbulent structures of the jets and the plate for larger hole. Indeed, for $h \leq 2D$, the jet mixing layers impinge on the plate and are strongly distorted by the impingement, whereas for $h \geq 3D$, they pass entirely through the hole and are almost unaffected. The interactions are especially weak for the largest hole $h = 4D$, resulting in a decrease by 4 dB of the overall acoustic level in the vicinity of the nozzle in comparison with the full-plate case. Moreover, for $h \leq 3D$, a hump is found at a low frequency in the near-nozzle pressure spectra. The peak frequency falls in the allowable frequency range of the upstream-propagating guided jet waves, which suggests that a feedback loop may establish between the nozzle and the plate. However, the peak is too wide and its amplitude is too low to definitely conclude about the existence of a feedback phenomenon in the present cases. The possibility of such a phenomenon and its related acoustic tones could be investigated in future work for rocket jets impinging on plates at a smaller nozzle-to-plate distance, typically $L = 15r_0$.

Acknowledgments

This work was financed by ArianeGroup and the Direction Générale de l'Armement (DGA). It was also financially supported by the IRICE IJES project RA0014963 (Installed Jet Effect Simulator, FEDER-FSE Rhône-Alpes). It was granted access to the HPC resources of Pôle de Modélisation et de Calcul en Sciences de l'Ingénieur et de l'Information (PMCS2I) of Ecole Centrale de Lyon, Pôle Scientifique de Modélisation Numérique (PSMN) of ENS de Lyon, members of Fédération Lyonnaise de Modélisation et Sciences Numériques (FLMSN), partner of EQUIPEX EQUIP@MESO, and to the resources of Institut du Développement et des Ressources en Informatique Scientifique (IDRIS) under the allocation 2021-2a0204 made by Grand Equipement National de Calcul Intensif (GENCI). It was performed within the framework of the LABEX CeLyA (ANR-10-LABX-0060) of Université de Lyon, within the program Investissements d'Avenir (ANR-16-IDEX-0005) operated by the French National Research Agency (ANR). The authors also gratefully acknowledge the Centre National d'Études Spatiales (CNES) for sharing the data of the MARTEL experiments.

References

- [1] Kawai, S., Tsutsumi, S., Takaki, R., and Fujii, K., "Computational Aeroacoustic Analysis of Overexpanded Supersonic Jet Impingement on a Flat Plate With/Without Hole," *ASME/JSM 2007 5th Joint Fluids Engineering Conference*, Paper FEDSM2007-37563, 2007,

- pp. 1163–1167.
<https://doi.org/10.1115/FEDSM2007-37563>
- [2] Tsutsumi, S., Takaki, R., Ikaida, H., and Terashima, K., “Numerical Aeroacoustics Analysis of a Scaled Solid Jet Impinging on Flat Plate with Exhaust Hole,” *30th International Symposium on Space Technology and Science*, Paper 2015-o-2-05, 2015.
 - [3] Troyes, J. N., Vuillot, F., Langenais, A., and Lambaré, H., “Coupled CFD-CAA Simulation of the Noise Generated by a Hot Supersonic Jet Impinging on a Flat Plate with Exhaust Hole,” *AIAA Paper 2019-2752*, 2019.
<https://doi.org/10.2514/6.2019-2752>
 - [4] Tsutsumi, S., Takaki, R., Shima, E., Fujii, K., and Arita, M., “Generation and Propagation of Pressure Waves from H-IIA Launch Vehicle at Lift-Off,” *AIAA Paper 2008-0390*, 2008.
<https://doi.org/10.2514/6.2008-390>
 - [5] Powell, A., “The Sound-Producing Oscillations of Round Underexpanded Jets Impinging on Normal Plates,” *Journal of the Acoustical Society of America*, Vol. 83, No. 2, 1988, pp. 515–533.
<https://doi.org/10.1121/1.396146>
 - [6] Tam, C., and Ahuja, K., “Theoretical Model of Discrete Tone Generation by Impinging Jets,” *Journal of Fluid Mechanics*, Vol. 214, May 1990, pp. 67–87.
<https://doi.org/10.1017/S0022112090000052>
 - [7] Norum, T. D., “Supersonic Rectangular Jet Impingement Noise Experiments,” *AIAA Journal*, Vol. 29, No. 7, 1991, pp. 1051–1057.
<https://doi.org/10.2514/3.10703>
 - [8] Tam, C., and Norum, T., “Impingement Tones of Large Aspect Ratio Supersonic Rectangular Jets,” *AIAA Journal*, Vol. 30, No. 2, 1992, pp. 304–311.
<https://doi.org/10.2514/3.10919>
 - [9] Umeda, Y., and Ishii, R., “Hole Tone Generation from Highly Choked Jets,” *Journal of the Acoustical Society of America*, Vol. 94, No. 2, 1993, pp. 1058–1066.
<https://doi.org/10.1121/1.406952>
 - [10] Henderson, B., Bridges, J., and Wernet, M., “An Experimental Study of the Oscillatory Flow Structure of Tone-Producing Supersonic Impinging Jets,” *Journal of Fluid Mechanics*, Vol. 542, Nov. 2005, pp. 115–137.
<https://doi.org/10.1017/S0022112005006385>
 - [11] Gojon, R., Bogey, C., and Marsden, O., “Investigation of Tone Generation in Ideally Expanded Supersonic Planar Impinging Jets Using Large-Eddy Simulation,” *Journal of Fluid Mechanics*, Vol. 808, Dec. 2016, pp. 90–115.
<https://doi.org/10.1017/jfm.2016.628>
 - [12] Bogey, C., and Gojon, R., “Feedback Loop and Upwind-Propagating Waves in Ideally Expanded Supersonic Impinging Round Jets,” *Journal of Fluid Mechanics*, Vol. 823, July 2017, pp. 562–591.
<https://doi.org/10.1017/jfm.2017.334>
 - [13] Varé, M., and Bogey, C., “Generation of Acoustic Tones in Round Jets at a Mach Number of 0.9 Impinging on a Plate with and Without a Hole,” *Journal of Fluid Mechanics*, Vol. 936, 2022, Paper A16.
<https://doi.org/10.1017/jfm.2022.47>
 - [14] Piantanida, S., and Berterretche, P., “Acoustic Characterization of Two Parallel Supersonic Jets,” *INTER-NOISE and NOISE-CON Congress and Conference Proceedings*, Vol. 259, 2019, pp. 4251–4262.
 - [15] Doty, M., and McLaughlin, D., “Acoustic and Mean Flow Measurements of High-Speed, Helium-Air Mixture Jets,” *International Journal of Aeroacoustics*, Vol. 2, No. 3, 2003, pp. 293–333.
<https://doi.org/10.1260/147547203322986151>
 - [16] Bogey, C., Marsden, O., and Bailly, C., “Large-Eddy Simulation of the Flow and Acoustic Fields of a Reynolds Number 10^5 Subsonic Jet with Tripped Exit Boundary Layers,” *Physics of Fluids*, Vol. 23, No. 3, 2011, Paper 035104.
<https://doi.org/10.1063/1.3555634>
 - [17] Liu, J., and Khine, Y.-Y., “Nozzle Boundary-Layer Separation Near the Nozzle Exit in Highly Overexpanded Jets,” *AIAA Paper 2020-2561*, 2020.
<https://doi.org/10.2514/6.2020-2561>
 - [18] Bogey, C., and Sabatini, R., “Effects of Nozzle-Exit Boundary-Layer Profile on the Initial Shear-Layer Instability, Flow Field and Noise of Subsonic Jets,” *Journal of Fluid Mechanics*, Vol. 876, Oct. 2019, pp. 288–325.
<https://doi.org/10.1017/jfm.2019.546>
 - [19] Bogey, C., “Acoustic Tones in the Near-Nozzle Region of Jets: Characteristics and Variations Between Mach Numbers 0.5 and 2,” *Journal of Fluid Mechanics*, Vol. 921, Aug. 2021.
<https://doi.org/10.1017/jfm.2021.426>
 - [20] Bogey, C., and Bailly, C., “A Family of Low Dispersive and Low Dissipative Explicit Schemes for Flow and Noise Computations,” *Journal of Computational Physics*, Vol. 194, No. 1, 2004, pp. 194–214.
<https://doi.org/10.1016/j.jcp.2003.09.003>
 - [21] Bogey, C., De Cacqueray, N., and Bailly, C., “A Shock-Capturing Methodology Based on Adaptive Spatial Filtering for High-Order Non-Linear Computations,” *Journal of Computational Physics*, Vol. 228, No. 5, 2009, pp. 1447–1465.
<https://doi.org/10.1016/j.jcp.2008.10.042>
 - [22] Fauconnier, D., Bogey, C., and Dick, E., “On the Performance of Relaxation Filtering for Large-Eddy Simulation,” *Journal of Turbulence*, Vol. 14, No. 1, 2013, pp. 22–49.
<https://doi.org/10.1080/14685248.2012.740567>
 - [23] Tam, C., and Dong, Z., “Radiation and Outflow Boundary Conditions for Direct Computation of Acoustic and Flow Disturbances in a Non Uniform Mean Flow,” *Journal of Computational Acoustics*, Vol. 4, No. 2, 1996, pp. 175–201.
<https://doi.org/10.1142/S0218396X96000040>
 - [24] Mohseni, K., and Colonius, T., “Numerical Treatment of Polar Coordinate Singularities,” *Journal of Computational Physics*, Vol. 157, No. 2, 2000, pp. 787–795.
<https://doi.org/10.1006/jcph.1999.6382>
 - [25] Bogey, C., De Cacqueray, N., and Bailly, C., “Finite Differences for Coarse Azimuthal Discretization and for Reduction of Effective Resolution Near Origin of Cylindrical Flow Equations,” *Journal of Computational Physics*, Vol. 230, No. 4, 2011, pp. 1134–1146.
<https://doi.org/10.1016/j.jcp.2010.10.031>
 - [26] Pineau, P., and Bogey, C., “Numerical Investigation of Wave Steepening and Shock coalescence Near a Cold Mach 3 Jet,” *Journal of the Acoustical Society of America*, Vol. 149, No. 1, 2021, pp. 357–370.
<https://doi.org/10.1121/10.0003343>
 - [27] Pineau, P., and Bogey, C., “Links Between Steepened Mach Waves and Coherent Structures for a Supersonic Jet,” *AIAA Journal*, Vol. 59, No. 5, 2021, pp. 1673–1681.
<https://doi.org/10.2514/1.J059859>
 - [28] De Cacqueray, N., Bogey, C., and Bailly, C., “Investigation of a High-Mach-Number Overexpanded Jet Using Large-Eddy Simulation,” *AIAA Journal*, Vol. 49, No. 10, 2011, pp. 2171–2182.
<https://doi.org/10.2514/1.J050952>
 - [29] Langenais, A., Vuillot, F., Troyes, J., and Bailly, C., “Accurate Simulation of the Noise Generated by a Hot Supersonic Jet Including Turbulence Tripping and Nonlinear Acoustic Propagation,” *Physics of Fluids*, Vol. 31, No. 1, 2019, Paper 016105.
<https://doi.org/10.1063/1.5050905>
 - [30] Nonomura, T., and Fujii, K., “Overexpansion Effects on Characteristics of Mach Waves from a Supersonic Cold Jet,” *AIAA Journal*, Vol. 49, No. 10, 2011, pp. 2282–2294.
<https://doi.org/10.2514/1.J051054>
 - [31] Pineau, P., and Bogey, C., “Steepened Mach Waves Near Supersonic Jets: Study of Azimuthal Structure and Generation Process Using Conditional Averages,” *Journal of Fluid Mechanics*, Vol. 880, Dec. 2019, pp. 594–619.
<https://doi.org/10.1017/jfm.2019.729>
 - [32] Seiner, J., and Yu, J., “Acoustic Near-Field Properties Associated with Broadband Shock Noise,” *AIAA Journal*, Vol. 22, No. 9, 1984, pp. 1207–1215.
<https://doi.org/10.2514/6.1981-1975>
 - [33] Tam, C., “Supersonic Jet Noise,” *Annual Review of Fluid Mechanics*, Vol. 27, No. 1, 1995, pp. 17–43.
<https://doi.org/10.1146/annurev.fl.27.010195.000313>
 - [34] Troyes, J., Vuillot, F., Lambaré, H., and Espinosa Ramos, A., “Numerical Study of Free Supersonic Hot Jet on Unstructured Grids with Emphasis on Aerodynamics and Resulting Radiated Noise,” *AIAA Paper 2016-2734*, 2016.
<https://doi.org/10.2514/6.2016-2734>
 - [35] Tam, C., and Tanna, H., “Shock Associated Noise of Supersonic Jets from Convergent-Divergent Nozzles,” *Journal of Sound and Vibration*, Vol. 81, No. 3, 1982, pp. 337–358.
[https://doi.org/10.1016/0022-460X\(82\)90244-9](https://doi.org/10.1016/0022-460X(82)90244-9)
 - [36] Pack, D., “A Note on Prandtl’s Formula for the Wave-Length of a Supersonic Gas Jet,” *Quarterly Journal of Mechanics and Applied Mathematics*, Vol. 3, No. 2, 1950, pp. 173–181.
<https://doi.org/10.1093/qjmath/3.2.173>
 - [37] Tam, C., Jackson, J., and Seiner, J., “A Multiple-Scales Model of the Shock-Cell Structure of Imperfectly Expanded Supersonic Jets,” *Journal of Fluid Mechanics*, Vol. 153, April 1985, pp. 123–149.
<https://doi.org/10.1017/S0022112085001173>
 - [38] Eggers, J., “Velocity Profiles and Eddy Viscosity Distributions Downstream of a Mach 2.22 Nozzle Exhausting to Quiescent Air,” *NASA TN D-3601*, 1966.
 - [39] Akamine, M., Nakanishi, Y., Okamoto, K., Teramoto, S., Okunuki, T., and Tsutsumi, S., “Acoustic Phenomena from Correctly Expanded Supersonic Jet Impinging on Inclined Plate,” *AIAA Journal*, Vol. 53,

- No. 7, 2015, pp. 2061–2067.
<https://doi.org/10.2514/1.J053953>
- [40] Akamine, M., Okamoto, K., Gee, K., Neilsen, T., Teramoto, S., Okunuki, T., and Tsutsumi, S., “Effect of Nozzle–Plate Distance on Acoustic Phenomena from Supersonic Impinging Jet,” *AIAA Journal*, Vol. 56, No. 5, 2018, pp. 1943–1952.
<https://doi.org/10.2514/1.J056504>
- [41] Nonomura, T., Goto, Y., and Fujii, K., “Aeroacoustic Waves Generated from a Supersonic Jet Impinging on an Inclined Flat Plate,” *International Journal of Aeroacoustics*, Vol. 10, No. 4, 2011, pp. 401–425.
<https://doi.org/10.1260/1475-472X.10.4.401>
- [42] Nonomura, T., Honda, H., Nagata, Y., Yamamoto, M., Morizawa, S., Obayashi, S., and Fujii, K., “Plate-Angle Effects on Acoustic Waves from Supersonic Jets Impinging on Inclined Plates,” *AIAA Journal*, Vol. 54, No. 3, 2015, pp. 816–827.
<https://doi.org/10.2514/1.J054152>
- [43] Harper-Bourne, M., and Fisher, M. J., “The Noise from Shock Waves in Supersonic Jets—Noise Mechanism,” AGARD Cp-131, 1974.
- [44] Bogey, C., Marsden, O., and Bailly, C., “Influence of Initial Turbulence Level on the Flow and Sound Fields of a Subsonic Jet at a Diameter-Based Reynolds Number of 10^5 ,” *Journal of Fluid Mechanics*, Vol. 701, June 2012, pp. 352–385.
<https://doi.org/10.1017/jfm.2012.162>
- [45] Nonomura, T., Nakano, H., Ozawa, Y., Terakado, D., Yamamoto, M., Fujii, K., and Oyama, A., “Large Eddy Simulation of Acoustic Waves Generated from a Hot Supersonic Jet,” *Shock Waves*, Vol. 29, March 2019, pp. 1133–1154.
<https://doi.org/10.1007/s00193-019-00895-2>
- [46] Bogey, C., and Pineau, P., “Potential-Core Closing of Temporally Developing Jets at Mach Numbers Between 0.3 and 2: Scaling and Conditional Averaging of Flow and Sound Fields,” *Physical Review Fluids*, Vol. 4, No. 12, 2019, Paper 124601.
<https://doi.org/10.1103/PhysRevFluids.4.124601>
- [47] Towne, A., Cavalieri, A. V. G., Jordan, P., Colonius, T., Schmidt, O., Jaunet, V., and Brès, G. A., “Acoustic Resonance in the Potential Core of Subsonic Jets,” *Journal of Fluid Mechanics*, Vol. 825, Aug. 2017, pp. 1113–1152.
<https://doi.org/10.1017/jfm.2017.346>
- [48] Brès, G., Jordan, P., Jaunet, V., Le Rallic, M., Cavalieri, A., Towne, A., Lele, S., Colonius, T., and Schmidt, O., “Importance of the Nozzle-Exit Boundary-Layer State in Subsonic Turbulent Jets,” *Journal of Fluid Mechanics*, Vol. 851, Sept. 2018, pp. 83–124.
<https://doi.org/10.1017/jfm.2018.476>
- [49] Tam, C., and Hu, F., “On the Three Families of Instability Waves of High-Speed Jets,” *Journal of Fluid Mechanics*, Vol. 201, April 1989, pp. 447–483.
<https://doi.org/10.1017/S002211208900100X>
- [50] Schmidt, O. T., Towne, A., Colonius, T., Cavalieri, A. V. G., Jordan, P., and Brès, G. A., “Wavepackets and Trapped Acoustic Modes in a turbulent Jet: Coherent Structure Eduction and Global Stability,” *Journal of Fluid Mechanics*, Vol. 825, Aug. 2017, pp. 1153–1181.
<https://doi.org/10.1017/jfm.2017.407>
- [51] Towne, A., Schmidt, O. T., and Brès, G. A., “An Investigation of the Mach Number Dependence of Trapped Acoustic Waves in Turbulent Jets,” *AIAA Paper 2019-2546*, 2019.
<https://doi.org/10.2514/6.2019-2546>
- [52] Sen, H. O., Seiler, F., Srulijes, J., and Hruschka, R., “Mach Waves Produced in the Supersonic Jet Mixing Layer by Shock/Vortex Interaction,” *Shock Waves*, Vol. 26, No. 3, 2016, pp. 231–240.
<https://doi.org/10.1007/s00193-015-0612-1>
- [53] Morris, P., “The Instability of High Speed Jets,” *International Journal of Aeroacoustics*, Vol. 9, Nos. 1–2, 2010, pp. 1–50.
<https://doi.org/10.1260/1475-472X.9.1-2.1>

M. M. Choudhari
 Associate Editor